Extreme Cold Winter Temperatures in Europe under the Influence of North Atlantic Atmospheric Blocking

Jana Sillmann, Mischa Croci-Maspoli, Malaak Kallache, Richard Katz

Extreme Cold Winter Temperatures in Europe under the Influence of North Atlantic Atmospheric Blocking

JANA SILLMANN*

Max Planck Institute for Meteorology, Hamburg, Germany

MISCHA CROCI-MASPOLI

Federal Office of Meteorology and Climatology, MeteoSwiss, Zurich, Switzerland

MALAAK KALLACHE

Laboratoire des Sciences du Climat et de l'Environnement (LSCE-IPSL), Gif-sur-Yvette, and Climpact, Paris, France

RICHARD W. KATZ

National Center for Atmospheric Research,+ Boulder, Colorado

(Manuscript received 16 September 2010, in final form 6 May 2011)

ABSTRACT

North Atlantic atmospheric blocking conditions explain part of the winter climate variability in Europe, being associated with anomalous cold winter temperatures. In this study, the generalized extreme value (GEV) distribution is fitted to monthly minima of European winter 6-hourly minimum temperatures from the ECHAM5/MPI-OM global climate model simulations and the ECMWF reanalysis product known as ERA-40, with an indicator for atmospheric blocking conditions being used as covariate. It is demonstrated that relating the location and scale parameter of the GEV distribution to atmospheric blocking improves the fit to extreme minimum temperatures in large areas of Europe. The climate model simulations agree reasonably with ERA-40 in the present climate (1961–2000). Under the influence of atmospheric blocking, a decrease in the 0.95th quantiles of extreme minimum temperatures can be distinguished. This cooling effect of atmospheric blocking is, however, diminished in future climate simulations because of a shift in blocking location, and thus reduces the chances of very cold winters in northeastern parts of Europe.

1. Introduction

Focusing on extreme cold temperatures seems not so compelling in the context of global warming. However, the recent winters serve as a good example of the impact of persistent cold outbreaks and anomalous snow amounts in Europe and North America, which posed a challenge for communities, transportation services, and the economy. Cattiaux et al. (2010), Seager et al. (2010), and Wang et al. (2010) have associated the anomalous winter of 2009/10 with large-scale atmospheric patterns or modes of climate variability, such as the North Atlantic Oscillation (NAO) and El Niño–Southern Oscillation (ENSO). Particularly the NAO, being in a very persistent negative phase, has contributed substantially to extreme cold spells in Europe. The negative NAO phase is also strongly associated with the occurrence of long-lasting (>10 days) atmospheric blocking conditions in the North Atlantic (Luo 2005; Schwierz et al. 2006), which was the case as well for the 2009/10 winter (cf. Fig. 1c in Cattiaux et al. 2010).

North Atlantic atmospheric blocking conditions in general disturb the predominant westerly flow over Europe, with the associated anticyclonic conditions

* Current affiliation: Canadian Centre for Climate Modeling and Analysis, University of Victoria, Victoria, British Columbia, Canada.

+ The National Center for Atmospheric Research is sponsored by the National Science Foundation.

Corresponding author address: Jana Sillmann, Canadian Centre for Climate Modeling and Analysis, University of Victoria, P.O. Box 3065 STN CSC, Victoria, BC V8W 3V6, Canada.
E-mail: jana.sillmann@ec.gc.ca

DOI: 10.1175/2011JCLI4075.1

allowing a northeasterly inflow of cold and dry air masses. Persistent clear-sky conditions favor increased outgoing longwave radiation during winter nights and result in a strong cooling of the earth surface and anomalous cold surface temperatures (e.g., Trigo et al. 2004). Sillmann and Croci-Maspoli (2009) further showed that atmospheric blocking conditions not only influence the mean winter climate, but also extreme cold temperature events in the Euro–Atlantic region. The latter study was based on indices for extreme events (Peterson 2005), which allow for a quantitative analysis provided the events are not too extreme.

Another way to investigate the influence of large-scale atmospheric patterns, or modes of climate variability, on extreme climate events is to include them as covariates in the statistical modeling of extreme values. This approach is based on extreme value theory (EVT), first popularized by Gumbel (1958). It enables a more sophisticated analysis of the characteristics of the probability distribution of extreme climate, including more efficient estimation of return values (i.e., an extreme event with a specified return period), a term that is often used in hydrology (e.g., ''100-yr flood'') for engineering design.

Classical EVT is based on the block maxima [the highest observed value of a climate variable within a certain time interval (year, season, month, etc.)], which follow under a wide range of conditions approximately the generalized extreme value (GEV) distribution [see Coles (2001) for more details]. As an alternative to the block maxima approach, the peaks-over-thresholds (POT) approach involves the generalized Pareto distribution (see Coles 2001), with the advantage of using more information about extremes in a given time period by modeling all values above a high threshold. One drawback of the POT, however, is its application to large (in spatial dimension) climate model datasets being more complicated, primarily because of the lack of automatic techniques for threshold selection (Davison and Smith 1990; Palutikof et al. 1999; Coles 2001). Thus, we will concentrate on the block maxima approach in this study.

EVT can also be extended to nonstationary processes enabling the inclusion of trends, as well as other more physically meaningful covariates (e.g., Coles 2001; Katz et al. 2002, 2005). These covariates can contribute to the frequency of occurrence and intensity of climate extremes. In this way, large-scale atmospheric patterns such as atmospheric blocking or the NAO, which explain a large part of the European climate variability (e.g., Scherrer et al. 2006), can be incorporated into the statistical modeling of climate extremes.

In climate applications, there have been several attempts to include such covariates in the GEV; most of them concentrated on observational data (e.g., Coles 2001; Katz et al. 2002; Chavez-Demoulin and Davison 2005; El Adlouni et al. 2007; Abeysirigunawardena et al. 2009; Maraun et al. 2010a; Zhang et al. 2010) and a few on coupled general circulation model (CGCM) output (e.g., Wang et al. 2004). This application of covariates based on large-scale atmospheric patterns, or modes of climate variability, is expected to improve the skill of statistical modeling of climate extremes, as would be valuable for statistical downscaling (e.g., Katz et al. 2002; Maraun et al. 2010b, 2011).

Hence, in the present study we want to investigate whether the statistical analysis of extreme winter temperature time series can be improved by conditioning the parameters of the GEV distribution on a covariate derived from an atmospheric blocking indicator. In particular, we use CGCM simulations and reanalysis to analyze the influence of North Atlantic atmospheric blocking events on the probability distribution of extreme cold temperatures in Europe under present and future climate conditions.

In section 2, we describe the CGCM simulations used for our analyses and introduce the blocking indicator in more detail. Section 3 concentrates on the methodology of extreme value analysis in terms of the GEV distribution for stationary and nonstationary processes. The results of our analysis are presented in section 4. In the last section, we draw conclusions and address problems associated with incorporating a covariate such as atmospheric blocking in the statistical modeling of climate extremes.

2. Model simulations and blocking indicator

a. ECHAM5/MPI-OM model simulations

We use climate simulations from the coupled general circulation model (CGCM) ECHAM5/MPI-OM (Jungclaus et al. 2006) developed at the Max Planck Institute for Meteorology (Hamburg, Germany). The atmospheric component of the CGCM (ECHAM5) (Roeckner et al. 2003) has a horizontal resolution of T63 in spectral space (corresponding to $1.875° \times 1.875°$ in gridbox space) and 31 vertical levels. The oceanic component (MPI-OM) (Marsland et al. 2003) is a z-coordinate circulation model with an integrated sea ice model and has a nominal horizontal resolution of 1.5° and 40 vertical levels. The coupling of the atmosphere to the ocean component requires no flux adjustments.

For our analyses, we use 6-hourly (2 m) minimum temperature (T2MIN) time series obtained from ensemble simulations (each with three ensemble members) of ECHAM5/MPI-OM for the present and future

climate. For the twentieth-century simulations, greenhouse gases (GHGs) and sulfate aerosols are prescribed according to observations and chemical transport model results, respectively. The scenario simulations are forced according to the Special Report on Emissions Scenarios (SRES) A1B, as described in Nakicenovic and Swart (2000). Each scenario ensemble member is a continuation of the corresponding twentieth-century ensemble member. The ensemble members of the present or future climate simulation differ slightly in their initial conditions and reflect independent realizations of the respective time period.

We concentrate on the winter months, December–February (DJF), in two 40-yr time slices: the first is taken from the present climate simulation ranging from 1961 to 2000 (hereafter 20C), and the second ranges from 2160 to 2199 and is taken from the stabilization period of the A1B scenario, when the atmospheric composition is kept constant at the level of year 2100 (hereafter A1B). In the stabilization period, the trends in temperature and precipitation due to increases in GHG concentrations are small relative to the trends simulated in the twenty-first century. Given these relatively small trends within the time slices, we concatenate the three ensemble members of the 20C and A1B simulation, respectively, to obtain a resulting time series of 120 years for each time period. These concatenated time series, referred to as $20C_{ens}$ and $A1B_{ens}$ in the following, represent the climate at the end of the twentieth century and at the end of the twenty-first century, respectively.

We also compare the 20C simulation of ECHAM5/MPI-OM with the European Centre for Medium-Range Weather Forecasts reanalysis product known as ERA-40 (Uppala et al. 2005) for the 1961–2000 time period.

b. The blocking indicator

To capture atmospheric blocking conditions in ECHAM5/MPI-OM, we apply a dynamical blocking indicator introduced by Schwierz et al. (2004). This indicator is calculated in two steps: first by computing the vertically averaged potential vorticity (PV) between 500 and 150 hPa and second by tracking the negative PV anomalies. Anomalies are calculated relative to the long-term climatology over the 1961–2000 and 2160–99 time period for ERA-40, 20C, and A1B. Structures of negative PV anomalies that have a minimum spatial extension of 1.8×10^6 km^2 and persist longer than 10 days are captured as a block at every instance of time (6 hourly). The blocking frequency (BF) is then defined as the percentage of the number of blocked days at a given grid box compared to a total number of days considered. For example, at a particular grid box a BF of 3% in a 31-day month would mean that blocking occurred for approximately 1 day in conjunction with an event with a lifetime of at least 10 days. We concentrate on these long-lasting blocking events, as they are statistically unusual compared to a simple red noise model (Woollings 2010).

This blocking indicator has proven valuable in climatological (Croci-Maspoli et al. 2007a,b) and also dynamical (Croci-Maspoli and Davies 2009; Altenhoff et al. 2008) studies. An important advantage of this PV-based blocking indicator is its ability to track blocking events of a particular length in space and time. Furthermore, the indicator has already been applied for future climate simulations of the ECHAM5/MPI-OM (Sillmann and Croci-Maspoli 2009), including a comparison between blocking events derived from ERA-40 data and present climate simulations.

In recent literature, CGCMs are often criticized for underestimating observed blocking frequencies (e.g., D'Andrea et al. 1998; Doblas-Reyes et al. 1998; Randall et al. 2007). Most of this deficiency can be directly attributed to the climatological bias of the model as revealed by Scaife et al. (2010). In their multimodel study, ECHAM5/MPI-OM produces a relatively small error in blocking frequencies compared to other CGCMs and observations, and the PV-based blocking indicator has also been shown to reduce the error in the mean model state.

c. Blocking climatology

The winter (DJF) blocking climatology of Euro–Atlantic domain (45°–75°N, 80°W–30°E) used in this study is shown in Fig. 1 for ERA-40 in comparison with the ECHAM5/MPI-OM ensemble simulations of 20C and A1B. In the following, the term "atmospheric blocking" refers to North Atlantic atmospheric blocking events occurring within this Euro–Atlantic domain.

The CGCM agrees well with ERA-40 in the spatial distribution and representation of blocking frequency in the present climate (Figs. 1a,b, left column). However, the center of maximum BF is located farther south in ECHAM5/MPI-OM, leading to higher BF between Iceland and the British Isles. In the future climate scenario A1B (Fig. 1c), we see a northward shift in the blocking location where the BF is diminished south of Greenland, but increased toward northwestern Canada in comparison with 20C. These changes in atmospheric blocking have also been revealed in other studies (e.g., Lupo et al. 1997; Bates and Meehl 1986). Matsueda et al. (2009) attribute the decrease in blocking frequencies under future climate conditions to an increase in the westerly jet over the North Atlantic. However, other dynamical processes (such as a poleward shift in the jet stream) could also lead to changes in BF and blocking

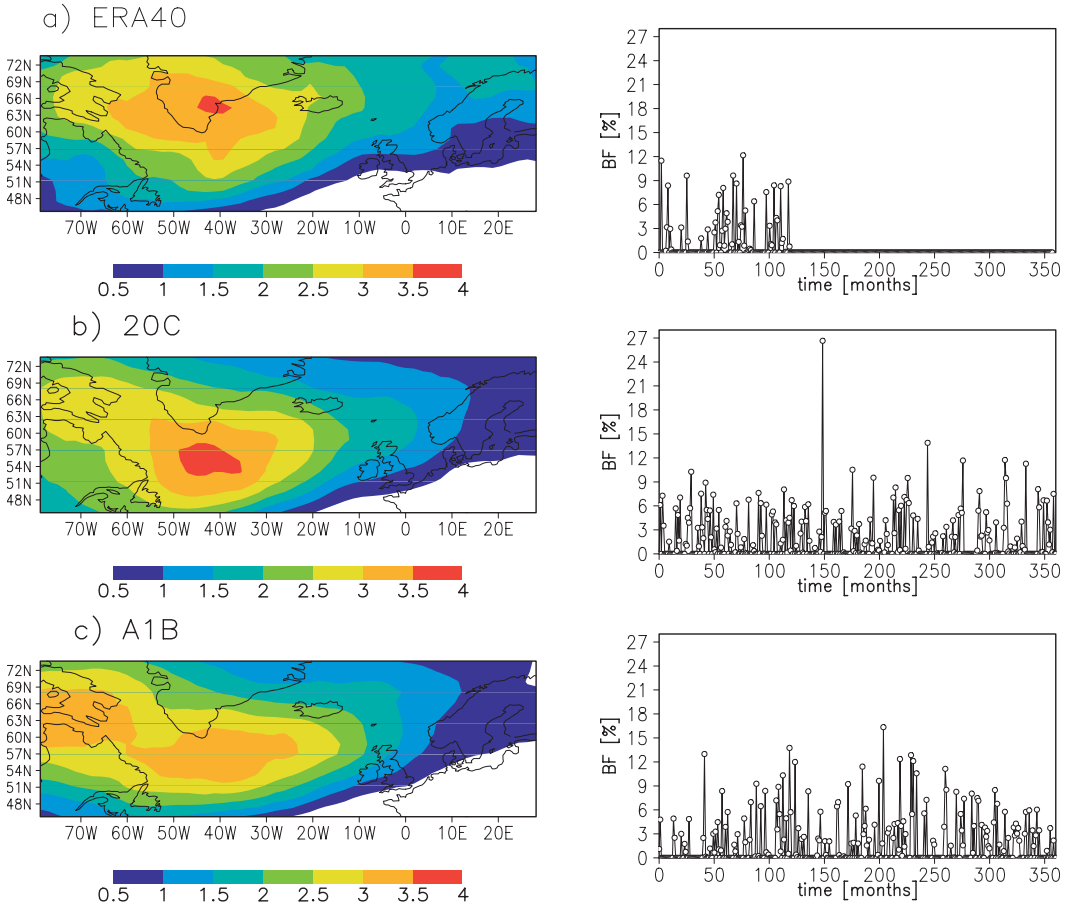

FIG. 1. (left) Temporal and (right) spatial averaged climatologies of the North Atlantic (45°–75°N, 80°W–30°E) atmospheric blocking frequencies (%) for (a) ERA-40 and (b) the 20C ensemble simulation (1961–2000) as well as (c) the A1B ensemble simulation (2160–99).

location over the North Atlantic, as discussed in Woollings et al. (2010).

When comparing the spatially averaged (Euro–Atlantic domain) climatologies as depicted in the right column of Fig. 1, we see that the BFs vary substantially over time with an average of 1.60%, 1.77%, and 1.69% for ERA-40, $20C_{ens}$, and $A1B_{ens}$, respectively. The time series of monthly averaged BFs serve as covariates in the statistical models described in section 3b. The maximum monthly BF is 12.2% in ERA-40, 26.6% in $20C_{ens}$, and 16.3% in $A1B_{ens}$. We interpret the large BF of 26.6% in one of the 20C ensemble members as an extreme event consistent with the climate variability in ECHAM5/MPI-OM under the prescribed GHG forcing.

3. Methodology

a. GEV for stationary processes

We briefly review the extreme value theory on which our assessment of extreme temperature events in CGCM simulations and reanalysis is based [for more details on extreme value analysis, see Coles (2001); for climate applications, see Katz et al. (2002)]. We follow the block maxima approach,

$$M_n = \max\{X_1, X_2, \ldots, X_n\}, \tag{1}$$

where M_n are the maxima drawn from a series of random variables X_i for $i = 1, \ldots, n$ over a time interval of fixed length (e.g., month, season, year). For the minima, we follow the approach outlined by Coles (2001), fitting the GEV distribution to the maxima of $Y_i = -X_i$ for $i = 1, \ldots, n$. Small values of X_i, hence correspond to large values of Y_i owing to the sign change. We draw the minima separately from the individual months of December–February, which represent a winter season. By applying a second negation after the analysis, we present the results in terms of the original minima (see Coles 2001).

According to the Fisher–Tippett theorem (Fisher and Tippett 1928), if the distribution of M_n asymptotically

TABLE 1. Model collection of the GEV distribution for the stationary (model 0) and nonstationary cases (model 1 and 2) and their corresponding degrees of freedom (DF).

Model	μ	σ	ξ	GEV function	DF
0	0	0	0	$F(\mathrm{x}) \sim \mathrm{GEV}(\mu, \sigma, \xi)$	3
1	CAB	0	0	$F(\mathrm{x}\|\mathrm{CAB}=z) \sim \mathrm{GEV}(\mu(z), \sigma, \xi)$	4
2	CAB	CAB	0	$F(\mathrm{x}\|\mathrm{CAB}=z) \sim \mathrm{GEV}(\mu(z), \sigma(z), \xi)$	5

(i.e., as the block size n goes to infinity and M_n is suitably normalized) converges toward a nondegenerate distribution function G, then G must be a member of the GEV family,

$$G(x) = \exp\{-[1 + \xi(x - \mu)/\sigma]^{-1/\xi}\}, \qquad (2)$$

defined on $\{x: 1 + \xi(x - \mu)/\sigma > 0\}$. The GEV distribution has three parameters, $\mu, \sigma > 0$, and ξ, that denote the location, scale, and shape, respectively. Generally speaking, the location parameter determines the overall position and the scale parameter the spread of the distribution. The shape parameter ξ characterizes the tail behavior of the distribution, distinguishing between three types: (i) the Gumbel distribution, (ii) the Weibull distribution, and (iii) the Fréchet distribution. We estimate the parameters of the GEV distribution by the method of maximum likelihood (ML) (see Coles 2001 for more details).

We fit the GEV distribution to block minima of the extreme winter T2MIN over land from the ECHAM5/MPI-OM ensemble simulations and ERA-40. We use the individual winter months (DJF) as time blocks, thus obtaining 120 monthly minima for ERA-40 from the 40-yr (1961–2000) minimum temperature time series and 360 monthly minima for $20C_{ens}$ (1961–2000) and $A1B_{ens}$ (2160–99). Although the rate of convergence to the GEV is relatively slow for variables such as temperature, the approximation is reasonably accurate, even on a monthly time scale (Leadbetter et al. 1983). In fact, the slow rate of convergence means that the approximation would not improve much for seasonal instead of monthly minima. The choice of monthly minima is based on being particularly interested in the influence of North Atlantic atmospheric blocking conditions that usually persist for less than a month. Thus, statistical results based on monthly minima can be more readily interpreted physically than those based on seasonal or annual minima.

The statistical significance of the observed differences between the GEV parameter estimates of $20C_{ens}$ and $A1B_{ens}$ is determined by using the corresponding standard errors to perform a z test based on a large sample normal approximation.

b. GEV for nonstationary processes

Extreme value theory as described in section 3a can be extended to nonstationary processes by including a covariate (e.g., Coles 2001). In our study we condition the distribution of monthly negated minima on a covariate derived from the atmospheric blocking indicator (see section 2b). We assume the relationship between the covariate atmospheric blocking (CAB) and the location and log-transformed [to ensure $\sigma(z) > 0$] scale parameter to be linear. That is, conditional on the value of the atmospheric blocking indicator, say CAB = z, we obtain a GEV distribution with parameters

$$\mu(z) = \beta_0 + \beta_1 z \quad \text{and} \qquad (3)$$

$$\ln\sigma(z) = \gamma_0 + \gamma_1 z. \qquad (4)$$

We consider a collection of nested models listed in Table 1, where one or more parameters of the GEV are conditioned on CAB. To determine which statistical model best describes the variability in the underlying data, we apply the deviance statistic [see appendix A and Coles (2001) for more details]. Conditioning the shape parameter on CAB did not improve the fit to the GEV distribution, and thus will not be discussed.

c. GEV quantiles or return values

Under the assumption of stationarity, extremes are often expressed in terms of return values. The T-yr return value X_T, which is defined as the $(1 - 1/T)$th quantile of the GEV distribution, is obtained by inverting the GEV cumulative distribution function [Eq. (2); see, e.g., Coles 2001]. In this study we also consider the conditional quantile function of the GEV distribution because the parameters vary over time depending on the value z assumed by the covariate, as in Eqs. (3) and (4),

$$X_T = \begin{cases} \mu(z) - \dfrac{\sigma(z)}{\xi}\left\{1 - \left[-\ln\left(1 - \dfrac{1}{T}\right)\right]^{-\xi}\right\}, & \xi \neq 0 \\ \mu(z) - \sigma(z)\ln\left[-\ln\left(1 - \dfrac{1}{T}\right)\right], & \xi = 0. \end{cases} \qquad (5)$$

As an example with a return period shorter than the length of the time slice, we concentrate on the 0.95th conditional quantile of the nonstationary GEV in our analysis (hereafter Q95), which would correspond to the T = 20-yr return period if the GEV were stationary (hereafter RV20). We calculate Q95 and RV20 for ERA-40 and the concatenated time series $20C_{ens}$ and

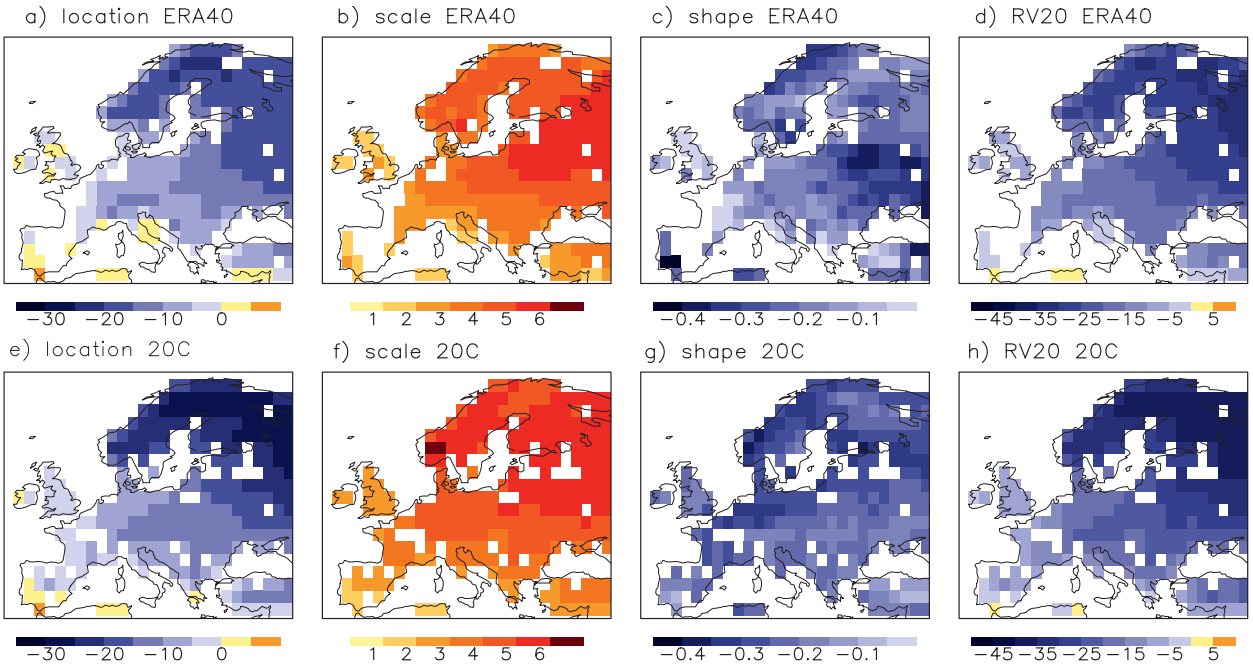

FIG. 2. GEV parameters [location (°C), scale (°C), and shape] and 20-yr return values RV20 (°C) for the DJF monthly minimum temperature extremes of the concatenated 20C ensemble members and the ERA-40 data for the time period 1961–2000. Grid boxes over land where the KS test failed are left blank.

$A1B_{ens}$ for the 1961–2000 and 2160–99 time periods, respectively. Confidence intervals for RV20 and Q95 in the present and future climate are calculated as described in appendix B.

4. Results and discussion

a. Stationary GEV

First we assess the goodness of fit of a GEV distribution for negated monthly minima by looking at quantile–quantile (Q–Q) plots to obtain a visual impression, as well as by performing a Kolmogorov–Smirnov (KS) test [as described in Kharin and Zwiers (2000) and Goubanova and Li (2007)]. The Q–Q plots (not shown) reveal that the quantiles of the fitted stationary and nonstationary GEV [Gumbel scaled, following Coles (2001)] are distributed closely around the diagonal line for the majority of grid boxes, indicating that the GEV distribution is a reasonably good fit to negated monthly T2MIN minima even for the upper tail of the distribution (i.e., the lower tail of minimum temperature).

In Fig. 2 we show a comparison between $20C_{ens}$ and ERA-40 of the GEV parameters and of the RV20 for the extreme T2MIN. Grid boxes over land, where the null hypothesis of the KS test (extremes are drawn from the fitted distribution) is rejected at the 5% significance level, remain blank. Since there are only very few boxes in Fig. 2 where the null hypotheses is rejected for $20C_{ens}$, the GEV distribution can be considered as an overall good representation of the extreme winter minimum temperature in Europe. For ERA-40, the KS test rejected the null hypothesis at most grid boxes over the Iberian Peninsula and northwestern France, indicating that the extreme T2MIN is not very well represented by the GEV distribution with one-month block length in this region.

In a comparison of $20C_{ens}$ with ERA-40 for the 1961–2000 time period as presented in Fig. 2, an overall good agreement in the spatial patterns of the estimated GEV parameters and RV20 can be seen for extreme T2MIN. There is a distinct north–south gradient with higher values in the south and lower in the north for the estimated location parameter (Figs. 2a,e) and a reversed gradient for the estimated scale parameter (Figs. 2b,f). This gradient reflects the overall spatial European temperature pattern with generally warmer temperatures and less variability in the south and colder temperatures and higher variability in the north. In northeastern Europe, however, the estimated location parameter of the GEV fitted to the 20C simulations is lower (−5°C on average) and the estimated scale parameter higher than for ERA-40. This indicates that ECHAM5/MPI-OM simulates colder extreme T2MIN with higher variability in northern latitudes than ERA-40. The difference in the estimated location parameter can be up to 9°C in northern Russia.

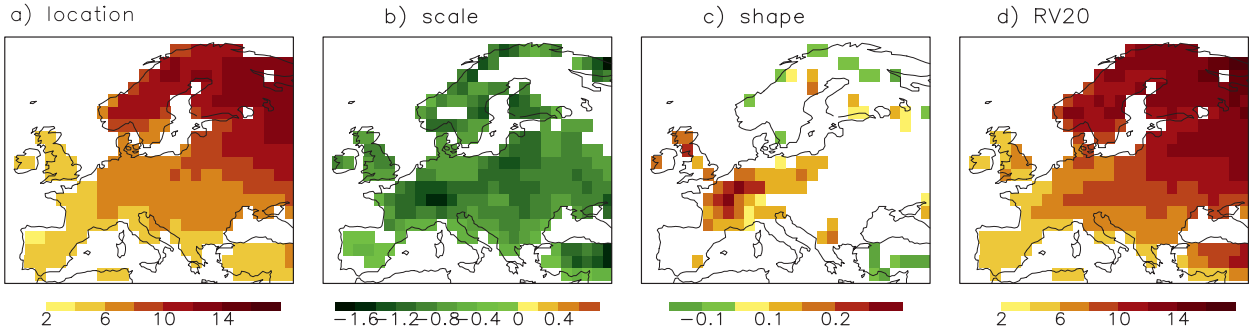

FIG. 3. Significant differences of the GEV parameters [location (°C), scale (°C), and shape] and RV20 (°C) for T2MIN between the concatenated ensemble members of the A1B (2160–99) and 20C (1961–2000) model simulations.

A possible reason for this bias could be the overestimation of winter sea level pressure in the Norwegian Sea and farther eastward (e.g., van Ulden and van Oldenborgh 2006), which leads to a weaker westerly flow and anomalous easterly winds in high northern latitudes resulting in anomalous cold winter temperature extremes in northeastern Europe. However, it should be noted that ERA-40 also has a bias at northern latitudes toward warmer winter surface air temperatures relative to observations (Hagemann et al. 2005). Furthermore, Sillmann and Roeckner (2008) showed in their study on indices for extremes that the index for the annual minimum of T2MIN obtained from ECHAM5/MPI-OM output agrees well with the index derived from observations from the Hadley Centre Global Climate Extremes dataset (HadEX). The cold bias in ECHAM5/MPI-OM is thus not as large as suggested from the comparison with ERA-40.

The estimated shape parameter (Figs. 2c,g) is always negative, indicating a Weibull type of GEV for $20C_{ens}$ and ERA-40 typical for temperature extremes in agreement with other studies (e.g., Kharin and Zwiers 2005; Parey 2008). RV20 (Figs. 2d,h), which involves the estimates of the three individual GEV parameters, also reveals a north–south gradient with lower values in the north and higher values in the south. The reduced location parameter over Scandinavia is also reflected in lower RV20 in $20C_{ens}$ compared to ERA-40.

We further assess differences in the estimated stationary GEV parameters and RV20 between present and future climate simulations as illustrated in Fig. 3. For the extreme T2MIN, we identified significant differences in the location parameter all over Europe. In A1B, the location parameter (Fig. 3a) indicates a strong temperature increase in northeastern Europe (12°–14°C) that decreases in magnitude toward southwestern Europe (2°–4°C). Goubanova and Li (2007) and Kharin et al. (2007) have also identified this pattern for other CGCMs, giving further confidence in our results. In addition, we found a significant decrease in the scale parameter (Fig. 3b) in large parts of Europe, indicating less variability in extreme T2MIN under future climate conditions. The latter result deviates from Kharin and Zwiers (2005) whose study indicates that future changes in extreme T2MIN in Europe are mainly governed by changes in the location and not the scale parameter. These differences are likely due to the different CGCM simulations utilized for the studies.

The estimated shape parameter (Fig. 3c) significantly increases, particularly in central Europe, but remains negative (−0.02) even for the greatest increase of 0.257 in this region. Thus, extreme T2MIN apparently remains distributed as the Weibull type of the GEV distribution in A1B.

The changes in the estimated RV20 (Fig. 3d) are significant throughout Europe and are comparable with the changes in the location parameter. There is a large increase in the return values (up to 16°C) in northeastern Europe and smaller increase toward southwestern Europe (5°C on average). This overall increase of RV20 would be consistent with an increased waiting time for extreme T2MIN events based on a fixed threshold.

b. Nonstationary GEV

In the following, we address two main issues by applying the nonstationary GEV distribution under present and future climate conditions: (i) to identify regions in Europe where CAB plays a statistically significant role in describing the underlying variability of extreme T2MIN by means of the deviance statistic and (ii) to quantify the effect of CAB on the parameters of the GEV distribution in these regions.

Including atmospheric blocking as a covariate in the GEV distribution results in nonstationary GEV parameters that vary over time according to the magnitude of CAB (cf. Fig. 1, right column). As an example of this procedure, we show a summary of the results of fitting different models (cf. Table 1) to the extreme T2MIN to

TABLE 2. Minimized negative log likelihoods (nllh) and parameter estimates with standard errors (SE) for the model collection (cf. Table 1) of the stationary (model 0) and nonstationary GEV distribution (models 1, 2) fitted to extreme T2MIN of $20C_{ens}$ for one grid box centered at 45.7°N, 7.5°E.

Model	nllh	μ (SE)		σ (SE)		ξ (SE)
0	983.96	−9.65 (0.21)		3.62 (0.15)		−0.23 (0.032)
1	980.24	−9.34 (0.24)	−0.18 (0.06)	3.58 (0.15)		−0.23 (0.034)
2	980.00	−9.34 (0.24)	−0.18 (0.06)	1.29 (0.05)	−0.009 (0.013)	−0.23 (0.033)

$20C_{ens}$ at one grid box centered at 45.7°N, 7.5°E in Table 2. Model 1 was selected as best model at this grid box according to the deviance statistic. Although model 2 has a slightly smaller nllh, the deviance [cf. Eq. (A1)] of $D = 0.48$ is not large enough on the scale of the χ^2 distribution to conclude that model 2 explains significantly more of the variability in the extreme T2MIN than does model 1.

As displayed in Fig. 4, the statistical model (cf. Table 1) selected as best at each grid box for $20C_{ens}$ is in agreement with that for ERA-40, with model 1 being selected in most parts of Europe. In other words, atmospheric blocking (linked to the location parameter) explains a significant part of the variability in the extreme T2MIN. Model 2 appears to be the best fitting model in southeastern Europe and northern Great Britain in ERA-40. For $20C_{ens}$, model 2 fits best in central Europe, reaching from northern France to northern Greece, and southwestern parts of the Iberian Peninsula. These spatial differences could be due to the differences in the spatial extension of the blocking climatology of ERA-40 and $20C_{ens}$ as shown in Fig. 1 (left column).

Under future climate conditions (A1B scenario, Fig. 4c), the influence of atmospheric blocking seems to diminish, with the stationary model being sufficient to explain the variability in extreme T2MIN in most of eastern Europe (most grid boxes east of 15°E). Model 1 is selected as best at most grid boxes between 0° and 15°E, whereas in southern Europe model 2 describes the extreme T2MIN best. The southwestward shift of the atmospheric blocking influence can be explained by the northward shift of the blocking distribution under future climate conditions as depicted in Fig. 1c (left column).

It is, however, difficult to physically interpret the regional differences in the selection of the statistical models 1 and 2 since CGCMs hardly replicate reality at these detailed scales. Thus, in the following, we will simplify the analysis by using only model 2 at all grid boxes where a nonstationary model was selected by the deviance statistic (cf. Fig. 4).

In Figs. 5a,b, the estimated slope of the location parameter at grid boxes where a nonstationary model was selected is negative for both $20C_{ens}$ and ERA-40. A negative slope implies that with increasing blocking frequency we can expect lower extreme T2MIN. For example, for a slope of −0.5°C we can expect a decrease in the GEV location parameter of 0.5°C per 1% increase in blocking frequency. In comparison with ERA-40 with a minimum slope of −0.57°C, the slopes are generally smaller in absolute magnitude in $20C_{ens}$ (minimum slope of −0.48°C). However, the spatial patterns are similar, with greatest absolute values of the slope along the south

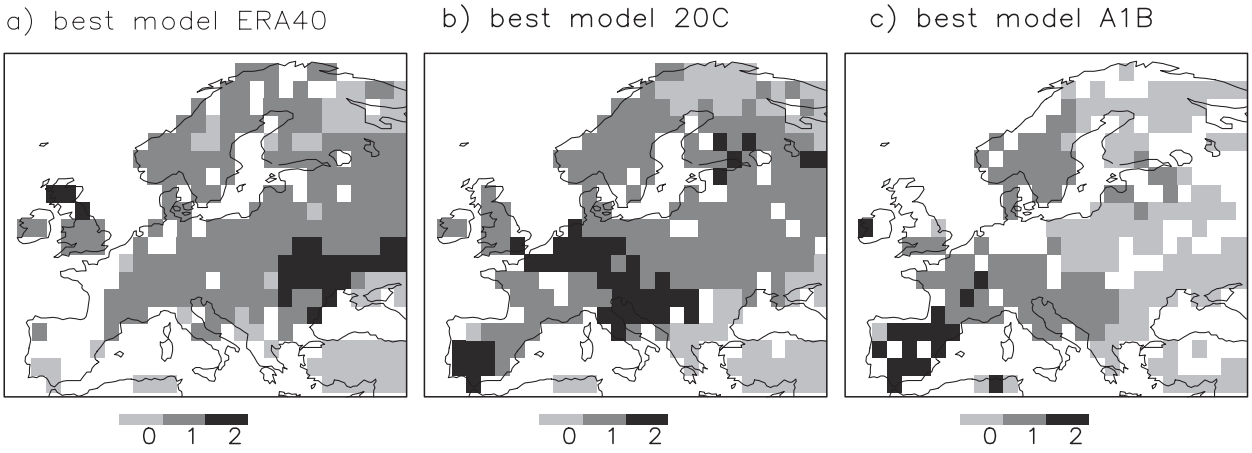

FIG. 4. Best statistical model (cf. Table 1) for (a) ERA-40 and the concatenated ensemble members of (b) 20C and (c) A1B according to the deviance statistic. Grid boxes over land where the KS test failed are left blank.

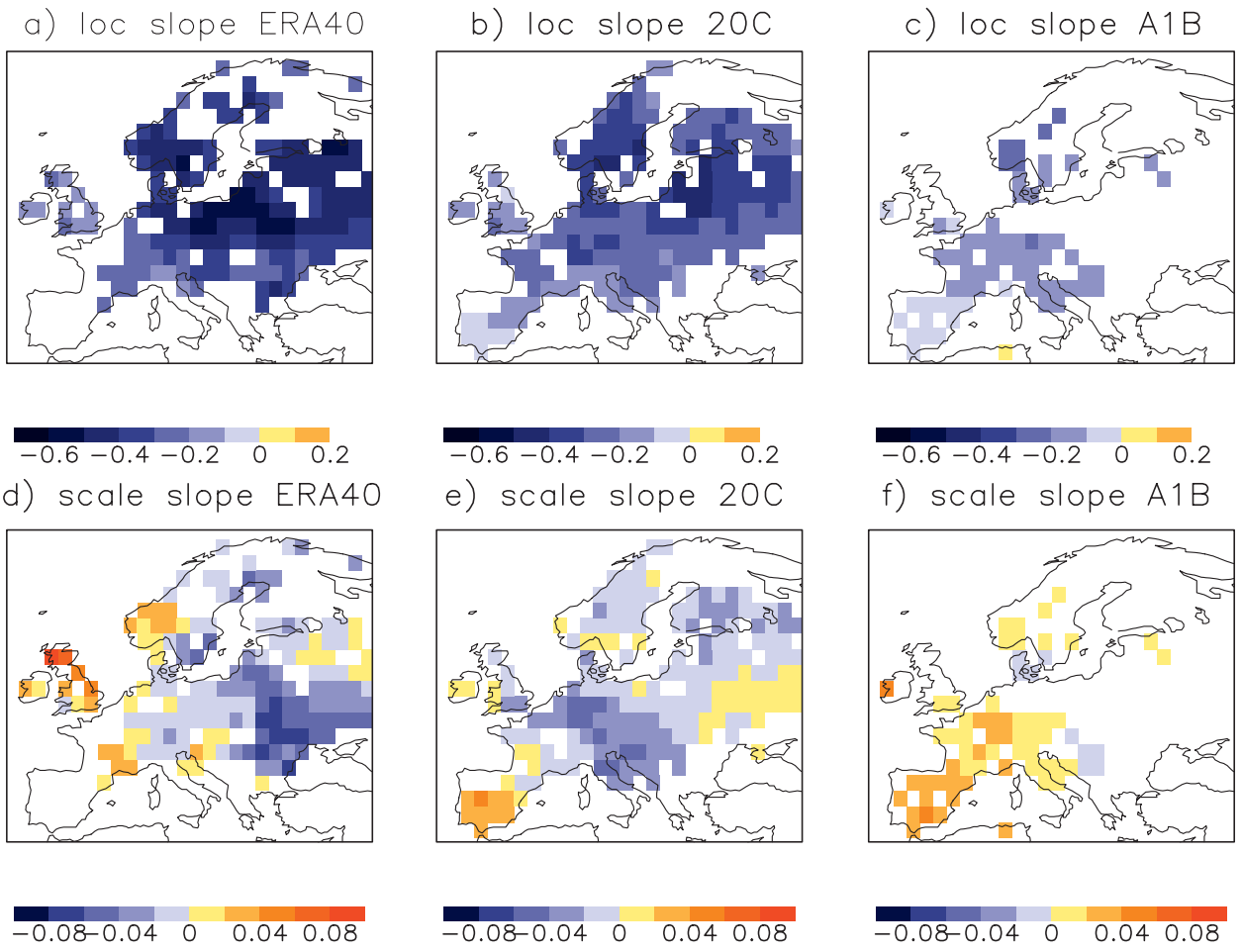

FIG. 5. (a)–(c) Slope of the location parameter β_1 (°C) and (d)–(f) slope of the log-transformed scale parameter γ_1 (°C) for the nonstationary GEV model 2 (cf. Table 1) for ERA-40 and the concatenated ensemble members of the 20C and A1B simulations.

coast of the Baltic Sea in both $20C_{ens}$ and ERA-40, indicating that atmospheric blocking has the greatest impact in northeastern Europe.

The slope of the estimated log-transformed scale parameter γ_1 is also generally negative in central and northeastern Europe, as shown in Figs. 5d,e for $20C_{ens}$ and ERA-40. However, γ_1 has a positive sign in southern Europe, particularly on the Iberian Peninsula in $20C_{ens}$. In other words, the variability of extreme T2MIN in southern Europe tends to increase, whereas it decreases toward central or northern Europe under the influence of atmospheric blocking. This behavior could partly be explained by different anomalies in the 500-hPa geopotential height and precipitation patterns governing months with high BF as revealed by a composite analysis [not shown, but see Sillmann and Croci-Maspoli (2009) for European blocks]. Southern Europe, in particular, lies on the interface between positive and negative flow and precipitation anomalies associated with atmospheric blocking in 20C, with this interface moving northeastward in A1B.

In the future climate simulation the slope for the estimated location parameter (Fig. 5c) remains negative, but has smaller absolute values than those in $20C_{ens}$ and ERA-40. Hence, the relationship between atmospheric blocking and extreme T2MIN remains similar under future climate conditions; namely, when atmospheric blocking occurs in A1B, we still can expect colder extreme nighttime temperatures. However, because the overall area of the influence of CAB will be decreased in A1B according to the models selected (cf. Fig. 4c), North Atlantic atmospheric blocking events will not necessarily play an important role in the variability of future extreme T2MIN in northeastern parts of Europe.

In the southwestern part of Europe, where the nonstationary models are still selected as the best in A1B, the slope in the estimated log-transformed scale parameter remains positive on the Iberian Peninsula and

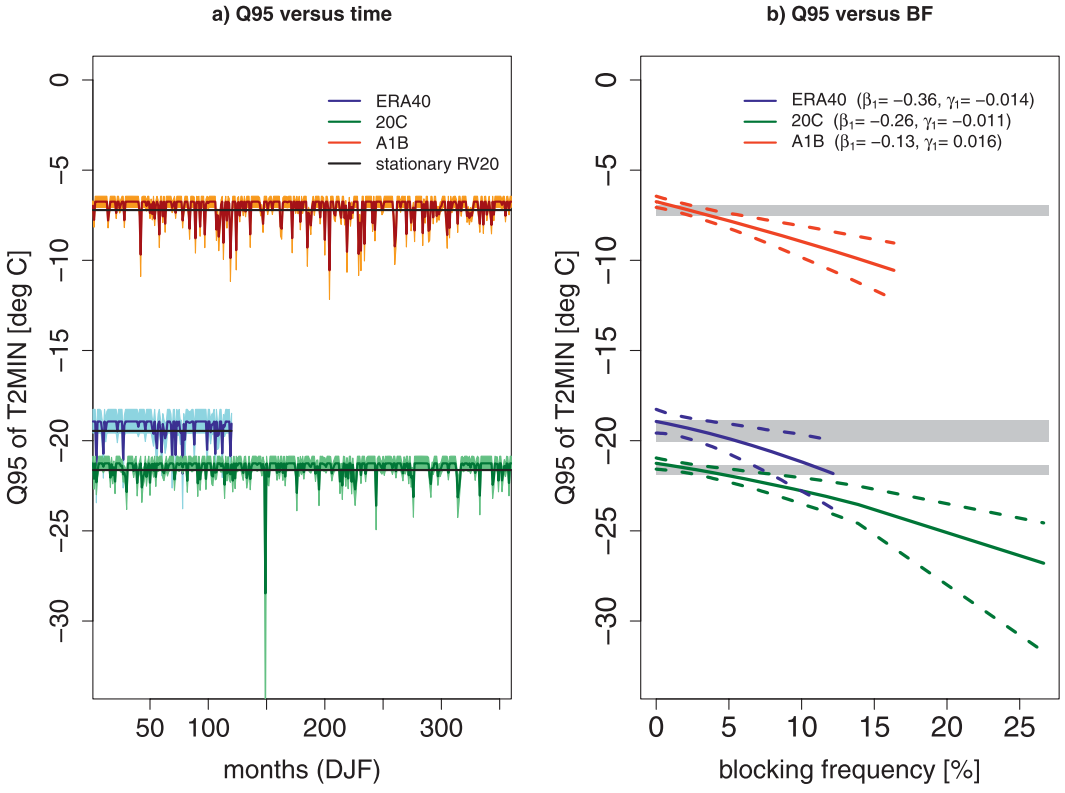

FIG. 6. Spatially averaged Q95 for regions where a nonstationary model was selected as best for ERA-40 (blue), $20C_{ens}$ (green), and $A1B_{ens}$ (red) and the corresponding RV20 (black horizontal lines). (a) Temporal evolution of Q95 vs blocking frequencies with $20C_{ens}$ and ERA-40 starting in year 1961 and $A1B_{ens}$ starting in year 2160. Light shading indicates the respective 80% confidence intervals. (b) Q95 vs blocking frequencies. The 80% confidence intervals are indicated for Q95 (dashed lines) and for the corresponding RV20 (horizontal shaded area).

changes from a negative to a positive sign farther eastward (Fig. 5f). The reason for this sign change has yet to be investigated. In general terms, an increase in the variability of extreme T2MIN can be expected over southwestern Europe in the future climate when atmospheric blocking occurs.

c. *GEV quantiles or return values*

In this section, we more closely examine the influence of CAB on Q95 for ERA-40 and the 20C and A1B ensemble simulations in comparison to RV20 in those regions where CAB has a statistically significant influence on extreme T2MIN. We spatially average Q95 or RV20 over all grid boxes for which a nonstationary model was selected (cf. Fig. 4). As already mentioned, we fit model 2 to all of those grid boxes to calculate the spatially averaged Q95 in the following analysis. The spatial averaging allows us to "borrow strength" in a statistical sense by combining information over a region with similar statistical characteristics (Katz 2010).

The parameters of the nonstationary GEV distribution, and hence Q95, vary over time according to the covariate at each time step. Figure 6a shows this temporal evolution of Q95 depending on the strength of the atmospheric blocking event in ERA-40, $20C_{ens}$, and $A1B_{ens}$. For small or zero blocking frequencies, Q95 does not differ significantly from RV20, but the higher the BF or the longer the atmospheric blocking event persists in the Euro–Atlantic domain, the stronger becomes its influence on the extreme T2MIN in Europe. In general, this means that under the influence of CAB we can expect colder Q95 than would be obtained by just considering a stationary model under present as well as future climate conditions.

We assessed the statistical significance of the differences between RV20 and Q95 at roughly the 10% level by comparing whether their 80% confidence intervals overlap [see appendix B and Kharin and Zwiers (2005)]. The difference between Q95 and RV20 becomes significant when the BFs are larger than 10% or 6.5% for 20C or A1B, respectively, as can be seen in Fig. 6b. Owing to the shorter sample length of ERA-40 (only 120 months instead of 360 for 20C and A1B), the 80% confidence intervals of Q95 are comparably wider and

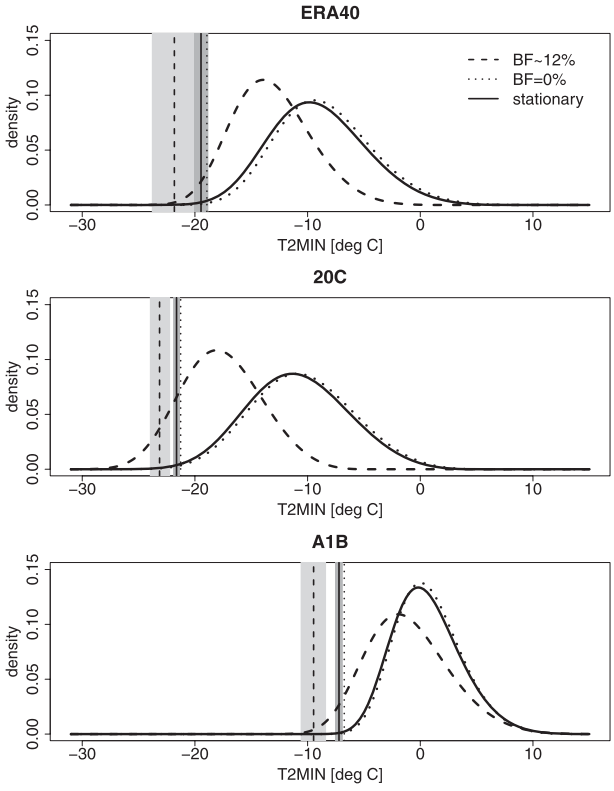

FIG. 7. Probability density functions of the stationary (solid) and nonstationary GEV for zero (dotted) and high blocking frequencies (dashed) of ERA-40, $20C_{ens}$, and $A1B_{ens}$, spatially averaged over regions where a nonstationary model was selected as best. Corresponding RV20 and Q95 for BF ~ 12% are indicated (vertical lines) with the respective 80% confidence intervals (gray shading).

the differences between RV20 and Q95 remain insignificant at the 10% level, even for maximum BF in ERA-40.

Figure 6b clearly shows the decrease of Q95 with increasing BF. The slope of the location parameter is, in absolute values, greatest for ERA-40 ($\beta_1 = -0.36$°C) and least for A1B ($\beta_1 = -0.13$°C). The 80% confidence intervals (indicated as dashed lines) widen with increasing BF because there are more zero and small BF values but only very few high BF values within the time periods. The linear relationship between the location parameter and CAB [cf. Eq. (3)] would correspond to a linear decrease in Q95 with increasing BF, but due to the relationship between the log-transformed scale parameter [cf. Eq. (4)] and CAB, the decrease is actually slightly nonlinear. The spatially averaged slope of the scale parameter γ_1 is negative for ERA-40 (−0.014°C) and $20C_{ens}$ (−0.011°C) and positive for $A1B_{ens}$ (0.016°C). In the regions where a positive γ_1 has been obtained (Fig. 5), the rate of decrease in Q95 with increasing BF is greater owing to the increase in variability of the conditional GEV distribution from the dependence of the scale parameter on CAB.

To analyze this aspect in more detail, we look at the spatially averaged estimated probability density functions (PDF) of the nonstationary and stationary GEV. Comparing the PDF of the stationary GEV with the nonstationary GEV for a month with high BF (~12%) and zero BF (Fig. 7), we can see a close resemblance between the stationary PDF (black) and the PDF for zero BF (green). The PDF for high BF (red) is, however, shifted to lower temperature values compared to zero BF or to the stationary GEV for ERA-40, $20C_{ens}$, and $A1B_{ens}$, emphasizing the importance of atmospheric blocking in explaining the variability of extreme T2MIN. Also, the corresponding Q95, as indicated by vertical dashed lines, are shifted to lower values of T2MIN for high BF compared to zero BF or RV20. This behavior follows directly from the relationship between the quantiles or return values (X_T) and the location parameter μ [Eq. (5)].

In regions where the estimated slope γ_1 is negative, the PDF narrows for high BF in comparison to zero BF or to the stationary GEV, as is evident in Fig. 7 for ERA-40 and 20C for which most of the grid boxes where a nonstationary model was selected have a negative γ_1. We see a widening of the PDF for high BF in regions with an estimated positive slope γ_1 of the log-transformed scale parameter, most obvious for A1B in Fig. 7 since only grid boxes with a positive slope in the estimated scale parameter were obtained in the future climate simulation (cf. Fig. 5). In general, a positive γ_1 leads to increased variability in the extreme T2MIN under the influence of CAB, as can be seen in the comparison of present and future climate conditions in Fig. 7 where for similar BF (~12%) the difference between RV20 and Q95 is greater for A1B with mainly positive γ_1 than for 20C with mainly negative γ_1.

We should point out that the influence of the scale parameter σ on the return values X_T depends on the chosen return period T as indicated in Eq. (5). Decreasing the return period T thus reduces the influence of σ on the return value X_T—in opposite direction to the influence of the location parameter μ. For example, if one chooses a return period smaller than 20 yr, for example, 2 yr (which corresponds to the median or 0.5th quantile of the distribution), we would obtain a different picture (not shown). The differences in 2-yr return values for the stationary and the nonstationary GEV distribution for high BF would be very small for positive values of γ_1 and larger for negative values.

In addition to the influence of atmospheric blocking on the extreme T2MIN, two other aspects are depicted by Figs. 6 and 7. First, we can see the cold bias in $20C_{ens}$ compared to ERA-40 (as already discussed in section 4a), indicated by the colder RV20 and Q95 in $20C_{ens}$

TABLE 3. Spatially averaged RV20 and Q95 (model 2 for BF ~ 12%) in degrees Celsius over all grid boxes in Europe for ERA-40, $20C_{ens}$, and $A1B_{ens}$ with the respective 0.1th and 0.9th quantiles given in parentheses.

	RV20	Q95
ERA-40	−17.7 (−16.8, −18.4)	−19.3 (−17.1, −21.1)
$20C_{ens}$	−21.3 (−20.8, −21.7)	−22.4 (−21.7, −23.4)
$A1B_{ens}$	−12.2 (−11.8, −12.6)	−13.0 (−12.1, −13.7)

compared to ERA-40 (see also Table 3). Second, and much more pronounced, we can see a shift of RV20 or Q95 and of the PDFs to warmer temperatures from 20C to A1B, reflected, for instance, by a warmer RV20 of −7°C in A1B and around −20°C in ERA-40 and $20C_{ens}$. Note that in these figures we are using the spatial averages of the areas where a nonstationary model was selected as best fitting according to the deviance statistic (cf. Fig. 4). Hence, the spatial averages of RV20 and Q95 in A1B are mainly derived from grid boxes in the southwestern part of Europe, which exhibits generally warmer winter T2MIN than the northeastern part. As seen in Table 3, the difference between A1B and 20C becomes somewhat smaller (by ~5°C) when averaging RV20 and Q95 (for BF ~ 12%) over all land grid boxes in Europe. But, the difference is still very significant, as the confidence intervals for RV20 or Q95 in A1B and 20C do not overlap for these spatial averages.

As part of the general warming trend under enhanced GHG, average waiting times for a particular cold extreme event will increase in the future climate scenario, meaning reduced chances for very cold winters. Atmospheric blocking still has a cooling effect on extreme T2MIN in future climate, as can be seen in by the decrease in Q95 for increasing blocking frequency (Fig. 6). However, this effect is small compared to the overall warming in Europe in A1B, which is reflected in the comparison between RV20 and Q95 for $20C_{ens}$ and $A1B_{ens}$ in Table 3. Especially in northeastern Europe, the cooling effect of atmospheric blocking is decreased under future climate conditions. The nonstationary models cannot explain a statistically significant part of the variability of extreme T2MIN in this region anymore, with the influence of atmospheric blocking diminishing as the blocking location shifts northward in A1B.

5. Summary and concluding remarks

In summary, the fit of the GEV distribution to negated extreme winter T2MIN can be significantly improved in large parts of Europe when atmospheric blocking is included as a covariate. In those regions with improved fit, we demonstrated a persistent negative relation between the location parameter and the CAB for ERA-40 as well as $20C_{ens}$ and $A1B_{ens}$. Especially for blocking frequencies above 10% in 20_{ens} and 6.5% in $A1B_{ens}$, the 0.95th quantile for the nonstationary GEV distribution is significantly reduced with respect to the 20-yr return value of the stationary GEV distribution. This effect is reinforced in regions where the scale parameter has a positive slope (e.g., in southern Europe). In winters with long-lasting atmospheric blocking events over the North Atlantic, we can expect significantly colder extreme nighttime temperatures in large parts of Europe. This response of extreme T2MIN to atmospheric blocking strengthens with increasing blocking frequency.

The relationship between extreme T2MIN and atmospheric blocking can also be seen under future climate conditions (A1B scenario), where we can still expect colder nighttime temperatures when persistent blocking events occur. However, the region where atmospheric blocking as a covariate can explain a significant part in the variability of extreme T2MIN is diminished in size to southwestern Europe as atmospheric blocking location shifts northward. Large areas in eastern and northern Europe are not significantly influenced by atmospheric blocking contributing to the general warming trend in T2MIN under enhanced GHG concentrations and reducing the chances of very cold winters.

As determined in the comparison of ECHAM5/MPI-OM with ERA-40, the representation of a large-scale atmospheric pattern, such as atmospheric blocking, can differ in location and magnitude between CGCM simulations and reanalysis [or observations as in Scaife et al. (2010)]. The results of the statistical modeling are also influenced by these differences and can, therefore, not be interpreted on small scales (e.g., grid boxes). Thus, the statistical modeling with covariates derived from large-scale atmospheric patterns can rather provide regional tendencies of the covariate's impact on a climate extreme. Improving the skill of CGCMs to represent, for instance, the blocking phenomenon correctly would increase the resolution at which the results of the statistical modeling of temperature extremes can be interpreted.

The PV-based atmospheric blocking indicator used in this study has emerged as a valuable tool for representing the dynamical features and the evolution of the blocking phenomenon. Thus, this indicator can be helpful for investigating the spatial dimension, geographical location, and time persistence of a blocking event that is most prominent for the occurrence of temperature extremes in Europe. In fact, the actual location of an atmospheric blocking event over the North Atlantic has an impact on how much the temperature extremes over Europe are affected. Blocking events occurring in the western Atlantic seem to have less influence on minimum

temperatures in Europe than blocking events closer to the continent, for example, the European blocks in Sillmann and Croci-Maspoli (2009).

Since atmospheric blocking explains only part of the variability of the European winter climate, the inclusion of other large-scale atmospheric patterns could probably further improve the fit of the GEV distribution to extreme T2MIN, explaining more of the variation in the data. However, given the limited data for extremes, models with several covariates are unlikely to be selected as best. A careful preselection of covariates is thus essential for the statistical modeling, depending on the climate extreme (e.g., T2MIN, T2MAX, precipitation, wind) and season under consideration.

Apart from considering more covariates, this study could be complemented by looking at more complex types of extreme temperature events such as cold spells, following the example of Furrer et al. (2010) for hot spells using the POT approach. This approach could also be useful when applying covariates that vary substantially on shorter time scales, such as North Atlantic atmospheric blocking conditions.

In general, the inclusion of covariates in the statistical modeling of climate extremes allows for the study of the relationship between a large-scale atmospheric pattern and the climate extreme. Such a relationship is manifested in time-dependent return values and thus raises various questions, such as how to treat this range of return values or what is the best choice of a return period. As we recognized in our study, the influence of the covariate on the climate extreme alters with the intensity of the covariate as well as with the chosen return period. Thus, when considering a nonstationary extreme value analysis we have to adjust the measures for risk assessment as established for the stationary extreme value analysis. In this respect, focusing on return values for a single return period might be misleading, with a detailed analysis of changes in the GEV density functions providing more information. These questions however can only be answered in close collaboration with studies concerning the impacts of climate extremes and concerning adaption and mitigation strategies for climate change impacts.

The overall promising benefit of the inclusion of covariates in the statistical modeling of climate extremes is the use of information on large-scale atmospheric patterns, which can be simulated more skillfully with CGCMs (van Ulden and van Oldenborgh 2006) than the climate extremes themselves. Improving the understanding of the interaction of covariates and climate extremes, such as the relationship between North Atlantic atmospheric blocking and European extreme minimum temperatures, could thus help us to project more reliably the occurrence and magnitude of such extreme events.

Acknowledgments. We greatly acknowledge Slava Kharin for his valuable comments on the methodology part. We also thank Michael Wehner, Francis Zwiers, and one anonymous reviewer for their comments that greatly improved the original manuscript. Further, we thank the ECMWF for providing the ERA-40 data. This work was supported by the International Max Planck Research School for Earth System Modeling and by the Canadian Foundation for Climate and Atmospheric Sciences through the CRCMD project.

APPENDIX A

Model Selection with Deviance Statistic

The deviance statistic D distinguishes between the negative log-likelihood (nllh) of two models, M_0 and M_1:

$$D = 2[\text{nllh}(M_0) - \text{nllh}(M_1)] > c_\alpha. \qquad \text{(A1)}$$

Let model M_0 be a subset of model M_1 by limiting the degrees of freedom (e.g., by constraining some of the parameters in M_1 to zero). This means that M_1 is the more complicated model with higher degrees of freedom.

The deviance statistic is, for a sufficiently large sample size, approximately χ^2_k distributed with k degrees of freedom under the assumption of M_0 being the correct model. Here k is equal to the difference in the number of free parameters of the two compared models. As described in Coles (2001), we can test the validity of model M_0 relative to M_1 at the α (=0.05) level of significance and reject M_0 in favor of M_1 if $D > c_\alpha$, where c_α is the $(1 - \alpha)$th quantile of this χ^2_k distribution.

APPENDIX B

Confidence Intervals for RV20 and Q95

For the stationary case, in which the parameters and thus RV20 remain constant over time, we determine significant differences by comparing whether the 80% confidence intervals for the 20C RV20 and A1B RV20 overlap. These confidence intervals are calculated using a parametric bootstrap approach (Efron and Tibshirani 1993) as follows. At each grid box, we generate 1000 samples of the length N of the original time series (N = 360 for $20C_{ens}$ and $A1B_{ens}$, N = 120 for ERA-40) using the parameters from a stationary GEV distribution fitted to the original data. The 0.1th and 0.9th quantiles of

the distribution of $RV20_i$ for $i = 1, \ldots, 1000$ derived from the generated samples are used then as lower and upper bounds for the 80% confidence interval of the RV20 from the initial sample. Comparing whether individual 80% confidence intervals overlap would correspond to a test of significance at roughly the 10% level (Kharin and Zwiers 2005).

For the spatial analysis in section 4c where we particularly concentrate on the time-varying Q95 for the nonstationary GEV distribution, we modify the resampling technique as described in Kharin and Zwiers (2005). Owing to the time-dependent parameters in the nonstationary case, the original data x_i for $i = 1, \ldots, N$ (with $N = 360$ for $20C_{ens}$ and A1B, $N = 120$ for ERA-40) needs to be transformed, for instance, by computing the residuals y_i, which are approximately identically distributed according to the Gumbel distribution with zero location and unit scale parameter:

$$y_i = \frac{1}{\hat{\xi}(z)} \ln\left\{1 + \hat{\xi}(z)\left[\frac{x_i - \hat{\mu}(z)}{\hat{\sigma}(z)}\right]\right\}, \qquad \text{(B1)}$$

where $\hat{\mu}(z)$, $\hat{\sigma}(z)$, and $\hat{\xi}(z)$ denote the estimated parameters for the best nonstationary model (cf. Table 1) selected at each grid box. To preserve spatial dependence, we resample with replacement the whole field of residuals y_i with the same best nonstationary model over the respective time period N. The 1000 generated samples are transformed [using the inverse of Eq. (B1)] to original fields with nonstationary GEV distribution as follows:

$$x_i = \hat{\mu}(z) - \frac{\hat{\sigma}(z)}{\hat{\xi}(z)}\{1 - \exp[\hat{\xi}(z)y_i]\}. \qquad \text{(B2)}$$

The GEV distribution of the best nonstationary model selected at each grid box is then fitted to the 1000 samples of x_i and $Q95_k$ for $k = 1, \ldots, 1000$. Finally, over all grid boxes with the same best nonstationary model selected, the 0.1th and 0.9th quantiles of the distribution of $Q95_k$ are used as lower and upper bounds for the 80% confidence interval of the spatially averaged Q95.

REFERENCES

Abeysirigunawardena, D. S., E. Gilleland, and D. Bronaugh, 2009: Extreme wind regime responses to climate variability and change in the inner south coast of British Columbia Canada. *Atmos.–Ocean,* **47,** 41–61.

Altenhoff, A. M., O. Martius, M. Croci-Maspoli, C. Schwierz, and H. C. Davies, 2008: Linkage of atmospheric blocks and synoptic-scale Rossby waves: A climatological analysis. *Tellus,* **60A,** 1053–1063, doi:10.1111/j.1600-0870.2008.00354.x.

Bates, G., and G. A. Meehl, 1986: The effect of CO_2 concentration on the frequency of blocking in a general circulation model coupled to a simple mixed layer ocean. *Mon. Wea. Rev.,* **114,** 687–701.

Cattiaux, J., R. Vautard, C. Cassou, P. Yiou, V. Masson-Delmotte, and F. Codron, 2010: Winter 2010 in Europe: A cold extreme in a warming climate. *Geophys. Res. Lett.,* **37,** L20704, doi:10.1029/2010GL044613.

Chavez-Demoulin, V., and A. C. Davison, 2005: Generalized additive modelling of sample extremes. *Appl. Stat.,* **54,** 207–222, doi:10.1111/j.1467-9876.2005.00479.x.

Coles, S., 2001: *An Introduction to Statistical Modeling of Extreme Values*. 1st ed. Springer Verlag, 224 pp.

Croci-Maspoli, M., and H. Davies, 2009: Key dynamical features of the 2005/06 European winter. *Mon. Wea. Rev.,* **137,** 644–678.

——, C. Schwierz, and H. C. Davies, 2007a: Atmospheric blocking: Space-time links to the NAO and PNA. *Climate Dyn.,* **29,** 713–725, doi:10.1007/s00382-007-0259-4.

——, ——, and ——, 2007b: A multifaced climatology of atmospheric blocking and its recent linear trend. *J. Climate,* **20,** 633–649.

D'Andrea, F., and Coauthors, 1998: Northern Hemisphere atmospheric blocking as simulated by 15 atmospheric general circulation models in the period 1979–1988. *Climate Dyn.,* **14,** 385–407.

Davison, A. C., and R. L. Smith, 1990: Models for exceedances over high thresholds. *J. Roy. Stat. Soc.,* **52B,** 393–442.

Doblas-Reyes, F. J., M. Deque, F. Valero, and D. B. Stephenson, 1998: North Atlantic wintertime intraseasonal variability and its sensitivity to GCM horizontal resolution. *Tellus,* **50A,** 573–595, doi:10.1034/j.1600-0870.1998.t01-4-00002.x.

Efron, B., and R. J. Tibshirani, 1993: *An Introduction to the Bootstrap*. *Statistics and Applied Probability Monogr.,* Vol. 57, Chapman and Hall/CRC, 456 pp.

El Adlouni, S., T. B. M. J. Ouarda, X. Zhang, R. Roy, and B. Bobee, 2007: Generalized maximum likelihood estimators for the non-stationary generalized extreme value model. *Water Resour. Res.,* **43,** W03410, doi:10.1029/2005WR004545.

Fisher, R. A., and L. H. C. Tippett, 1928: Limiting forms of the frequency distributions of the largest or smallest number of a sample. *Proc. Cambridge Philos. Soc.,* **24,** 180–190.

Furrer, E. M., R. W. Katz, M. D. Walter, and R. Furrer, 2010: Statistical modeling of hot spells and heat waves. *Climate Res.,* **43,** 191–205, doi:10.3354/cr00924.

Goubanova, K., and L. Li, 2007: Extremes in temperature and precipitation around the Mediterranean basin in an ensemble of future scenario simulations. *Global Planet. Change,* **57,** 27–42.

Gumbel, E. J., 1958: *Statistics of Extremes*. Columbia University Press, 375 pp.

Hagemann, S., K. Arpe, and L. Bengtsson, 2005: Validation of the hydrological cycle of ERA-40. Max Planck Institute for Meteorology, Earth System Science Rep. 10, 53 pp. [Available online at http://www.mpimet.mpg.de/fileadmin/publikationen/erdsystem_10.pdf.]

Jungclaus, J. H., and Coauthors, 2006: Ocean circulation and tropical variability in the coupled model ECHAM5/MPI-OM. *J. Climate,* **19,** 3952–3972.

Katz, R. W., 2010: Statistics of extremes in climate change. *Climatic Change,* **100,** 71–76, doi:10.1007/s10584-010-9834-5.

——, M. B. Parlange, and P. Naveau, 2002: Statistics of extremes in hydrology. *Adv. Water Resour.,* **25,** 1287–1304, doi:10.1016/S0309-1708(02)00056-8.

——, G. S. Brush, and M. B. Parlange, 2005: Statistic of extremes: Modeling ecological disturbances. *Ecology,* **86,** 1124–1134.

Kharin, V. V., and F. W. Zwiers, 2000: Changes in the extremes in an ensemble of transient climate simulations with a coupled atmosphere–ocean GCM. *J. Climate,* **13,** 3760–3788.

——, and ——, 2005: Estimating extremes in transient climate change simulations. *J. Climate,* **18,** 1156–1173.

——, ——, X. Zhang, and G. C. Hegerl, 2007: Changes in temperature and precipitation extremes in the IPCC ensemble of global coupled model simulations. *J. Climate,* **20,** 1419–1444.

Leadbetter, M. R., G. Lindgren, and H. Rootzen, 1983: *Extremes and Related Properties of Random Sequences and Processes*. Springer Verlag, 336 pp.

Luo, D., 2005: Why is the North Atlantic block more frequent and long-lived during the negative NAO phase? *Geophys. Res. Lett.,* **32,** L20804, doi:10.1029/2005GL022927.

Lupo, A. R., R. J. Oglesby, and I. I. Mokhov, 1997: Climatological features of blocking anticyclones: A study of Northern Hemisphere CCM1 model blocking events in present-day and double CO_2 concentration atmospheres. *Climate Dyn.,* **13,** 181–195.

Maraun, D., H. W. Rust, and T. J. Osborn, 2010a: Synoptic airflow and UK daily precipitation extremes. *Extremes,* **13,** 133–153, doi:10.1007/s10687-010-0102-x.

——, and Coauthors, 2010b: Precipitation downscaling under climate change: Recent developments to bridge the gap between dynamical models and the end user. *Rev. Geophys.,* **48,** RG3003, doi:10.1029/2009RG000314.

——, T. J. Osborn, and H. W. Rust, 2011: The influence of synoptic airflow on UK daily precipitation extremes. Part I: Observed spatio-temporal relations. *Climate Dyn.,* **36,** 261–275, doi:10.1007/s00382-009-0710-9.

Marsland, J. S., H. Haak, J. H. Junclaus, M. Latif, and F. Roeske, 2003: The Max Planck Institute global ocean/sea ice model with orthogonal curvilinear coordinates. *Ocean Modell.,* **5,** 91–127.

Matsueda, M., R. Mizuta, and S. Kusunoki, 2009: Future change in wintertime atmospheric blocking simulated using a 20-km-mesh atmospheric global circulation model. *J. Geophys. Res.,* **114,** D12114, doi:10.1029/2009JD011919.

Nakicenovic, N., and R. Swart, 2000: *Special Report on Emission Scenarios*. Cambridge University Press, 612 pp.

Palutikof, J. P., B. B. Brabson, D. H. Lister, and S. T. Adcock, 1999: A review of methods to calculate extreme wind speeds. *Meteor. Appl.,* **6,** 119–132.

Parey, S., 2008: Extremely high temperatures in France at the end of the century. *Climate Dyn.,* **30,** 99–112, doi:10.1007/s00382-007-0275-4.

Peterson, T. C., 2005: Climate change indices. *WMO Bull.,* **54,** 83–86.

Randall, D., and Coauthors, 2007: Climate models and their evaluation. *Climate Change 2007: The Physical Science Basis,* S. Solomon et al., Eds., Cambridge University Press, 589–662.

Roeckner, E., and Coauthors, 2003: The atmospheric general circulation model ECHAM5. Part 1: Model description. Max Planck Institute for Meteorology Rep. 349, 140 pp. [Available online at http://www.mpimet.mpg.de/fileadmin/publikationen/Reports/max_scirep_349.pdf.]

Scaife, A. A., T. Woollings, J. Knight, G. Martin, and T. Hinton, 2010: Atmospheric blocking and mean biases in climate models. *J. Climate,* **23,** 6143–6152.

Scherrer, S. C., M. Croci-Maspoli, C. Schwierz, and C. Appenzeller, 2006: Two-dimensional indices of atmospheric blocking and their statistical relationship with winter climate patterns in the Euro-Atlantic region. *Int. J. Climatol.,* **26,** 233–249.

Schwierz, C., M. Croci-Maspoli, and H. C. Davies, 2004: Perspicacious indicators of atmospheric blocking. *Geophys. Res. Lett.,* **31,** L06125, doi:10.1029/2003GL019341.

——, C. Appenzeller, H. C. Davies, M. A. Liniger, W. Müller, T. F. Stocker, and M. Yoshimori, 2006: Challenges posed by and approaches to the study of seasonal-to-decadal climate variability. *Climatic Change,* **79,** 31–63, doi:10.1007/s10584-006-9076-8.

Seager, R., Y. Kushnir, J. Nakamura, M. Ting, and N. Naik, 2010: Northern Hemisphere winter snow anomalies: ENSO, NAO and the winter of 2009/10. *Geophys. Res. Lett.,* **37,** L14703, doi:10.1029/2010GL043830.

Sillmann, J., and E. Roeckner, 2008: Indices for extreme climate events in projections of anthropogenic climate change. *Climatic Change,* **86,** 83–104.

——, and M. Croci-Maspoli, 2009: Present and future atmospheric blocking and its impact on European mean and extreme climate. *Geophys. Res. Lett.,* **36,** L10702, doi:10.1029/2009GL038259.

Trigo, R., I. Trigo, C. D. Camara, and T. J. Osborn, 2004: Climate impact of the European winter blocking episodes from the NCEP/NCAR Re-analysis. *Climate Dyn.,* **23,** 17–28.

Uppala, S. M., and Coauthors, 2005: The ERA-40 Re-Analysis. *Quart. J. Roy. Meteor. Soc.,* **131,** 2961–3012, doi:10.1256/qj.04.176.

van Ulden, A. P., and G. J. van Oldenborgh, 2006: Large-scale atmospheric circulation biases and changes in global climate model simulations and their importance for climate change in central Europe. *Atmos. Chem. Phys.,* **6,** 863–881.

Wang, C., H. Liu, and S. Lee, 2010: The record-breaking cold temperatures during the winter of 2009/2010 in the Northern Hemisphere. *Atmos. Sci. Lett.,* **11,** 161–168, doi:10.1002/asl.278.

Wang, X. L., F. W. Zwiers, and V. R. Swail, 2004: North Atlantic Ocean wave climate change scenarios for the twenty-first century. *J. Climate,* **17,** 2368–2383.

Woollings, T., 2010: Dynamical influences on European climate: An uncertain future. *Philos. Trans. Roy. Soc. London,* **368A,** 3733–3756.

——, A. Hannachi, and B. Hoskins, 2010: Variability of the North Atlantic eddy-driven jet stream. *Quart. J. Roy. Meteor. Soc.,* **136,** 856–868, doi:10.1002/qj.625.

Zhang, X., J. Wang, F. W. Zwiers, and P. Y. Groisman, 2010: The influence of large-scale climate variability on winter maximum daily precipitation over North America. *J. Climate,* **23,** 2902–2915.